

Animatable 3D Gaussian: Fast and High-Quality Reconstruction of Multiple Human Avatars

Yang Liu*
liu-yang22@mails.tsinghua.edu.cn
Tsinghua Shenzhen International
Graduate School
Shenzhen, China

Xiang Huang*
xiang.huang@galasports.com
Tsinghua Shenzhen International
Graduate School
Shenzhen, China
GalaSports
Shenzhen, China

Minghan Qin
qmh21@mails.tsinghua.edu.cn
Tsinghua Shenzhen International
Graduate School
Shenzhen, China

Qinwei Lin
lqw22@mails.tsinghua.edu.cn
Tsinghua Shenzhen International
Graduate School
Shenzhen, China

Haoqian Wang[†]
wanghaoqian@tsinghua.edu.cn
Tsinghua Shenzhen International
Graduate School
Shenzhen, China



Figure 1: Novel View Synthesis from Multi-View Video. We present novel view synthesis results of our proposed Animatable 3D Gaussian on single-human, double-human, and multi-human scenes. Our method can produce higher quality synthesis results than InstantAvatar [26] with only a few seconds of training time, and render novel view images at real-time speed. Moreover, our method requires a very small amount of GPU memory. We implement all experiments only on a single RTX 3090.

Abstract

Neural radiance fields are capable of reconstructing high-quality drivable human avatars but are expensive to train and render and not suitable for multi-human scenes with complex shadows. To reduce consumption, we propose Animatable 3D Gaussian, which learns human avatars from input images and poses. We extend 3D Gaussians to dynamic human scenes by modeling a set of skinned 3D Gaussians and a corresponding skeleton in canonical space and deforming 3D Gaussians to posed space according to the input

poses. We introduce a multi-head hash encoder for pose-dependent shape and appearance and a time-dependent ambient occlusion module to achieve high-quality reconstructions in scenes containing complex motions and dynamic shadows. On both novel view synthesis and novel pose synthesis tasks, our method achieves higher reconstruction quality than InstantAvatar with less training time (1/60), less GPU memory (1/4), and faster rendering speed (7×). Our method can be easily extended to multi-human scenes and achieve comparable novel view synthesis results on a scene with ten people in only 25 seconds of training. For video and code, please see <https://jimyyliu.github.io/Animatable-3D-Gaussian/>.

*Both authors contributed equally to this research.

[†]Corresponding author.

Permission to make digital or hard copies of all or part of this work for personal or classroom use is granted without fee provided that copies are not made or distributed for profit or commercial advantage and that copies bear this notice and the full citation on the first page. Copyrights for third-party components of this work must be honored. For all other uses, contact the owner/author(s).

MM '24, October 28–November 1, 2024, Melbourne, VIC, Australia

© 2024 Copyright held by the owner/author(s).

ACM ISBN 979-8-4007-0686-8/24/10

<https://doi.org/10.1145/3664647.3680674>

CCS Concepts

• Computing methodologies → Animation; Computer vision.

Keywords

Human Reconstruction, 3D Gaussian Splatting, Neural Radiance field

ACM Reference Format:

Yang Liu, Xiang Huang, Minghan Qin, Qinwei Lin, and Haoqian Wang. 2024. Animatable 3D Gaussian: Fast and High-Quality Reconstruction of Multiple Human Avatars. In *Proceedings of the 32nd ACM International Conference on Multimedia (MM '24), October 28–November 1, 2024, Melbourne, VIC, Australia*. ACM, New York, NY, USA, 10 pages. <https://doi.org/10.1145/3664647.3680674>

1 Introduction

Real-time rendering and fast reconstruction of a high-quality digital human has a variety of applications in various fields, such as virtual reality, gaming, sports broadcasting, and telepresence. Existing methods often take considerable time for training, and none of them can achieve high-quality reconstruction and real-time rendering in a very short training time.

Recent methods [5, 26, 37] implicitly reconstruct high-quality human avatars using neural radiance fields [35]. However, implicit neural radiance fields inevitably lead to artifacts in the synthesized novel views as they require modeling the entire space including empty space. Some of these methods [5, 37] require high memory and time consumption due to multilayer perceptron and complex point sampling for each ray. When it comes to datasets with dynamic illumination and shadow, the reconstruction quality of these methods [5, 26, 37] is significantly degraded. This decline is attributed to the inherent incapacity of these methods to accommodate the dynamic alterations in illumination and shadow.

In this paper, we aim to acquire high-fidelity human avatars from a monocular or sparse-view video sequence in seconds and to render high-quality novel views and poses at interactive rates (170 FPS for 540×540 resolution). To this end, we introduce a novel neural representation using 3D Gaussians (3D-GS [28]) for dynamic humans, named Animatable 3D Gaussian, overcoming the problem of artifacts in implicit neural radiance fields. In order to deform 3D Gaussians to the posed space, we model a set of skinned 3D Gaussians and a corresponding skeleton in canonical space. We use the multi-head hash encoder to encode the shape and appearance of 3D Gaussians to accelerate convergence speed, avoid overfitting, and acquire pose-dependent deformation. For low memory and time consumption of rendering, we use the 3D Gaussian rasterizer [28] to rasterize the deformed 3D Gaussians instead of volume rendering. To handle the dynamic illumination and shadow, we suggest modeling time-dependent ambient occlusion for each timestamp.

Since the public dataset [1, 37] contains few pose and shadow changes, we create a new dataset named GalaBasketball in order to show the performance of our method under complex motion and dynamic shadows. We evaluate our method on both public and our created dataset and compare it with state-of-the-art methods [5, 26]. Our method is able to reconstruct better-quality human avatars in a shorter time. Moreover, our method can be extended to multi-human scenes and performs well.

In summary, the major contributions of our work are:

- We propose Animatable 3D Gaussian, a novel neural representation using 3D Gaussians for dynamic humans, which reconstructs human avatars from scratch **without shape prior** such as SFM[41] or SMPL[33] shape parameters.
- We present a novel pipeline for human reconstruction that can acquire higher-fidelity human avatars with **lower memory and time consumption (few seconds)** than state-of-the-art methods [5, 26].
- We propose a time-dependent ambient occlusion module to reconstruct the dynamic shadows, which allows our method to obtain high-fidelity human avatars from **multi-human scenes** with complex motions and dynamic shadows.

2 Related Work

3D Human Reconstruction. Reconstructing 3D human has been a popular research topic in recent years. Traditional methods achieve high-fidelity reconstruction by means of depth sensors [9, 14, 19, 42] and dense camera arrays [11, 12], but expensive hardware requirements limit the application of these methods. Recent methods [1, 2, 18, 20, 21, 47, 48] utilized parametric mesh templates as a prior, such as SMPL [33]. By optimizing mesh templates, these methods are able to reconstruct 3D human bodies of different shapes. However, they have limitations in reconstructing details such as hair and fabric.

The emergence of neural radiance fields [35] has made neural representations popular in the field of human reconstruction. Many works [3, 5–8, 10, 13, 15, 22–27, 29, 32, 34, 37, 39, 40] have used neural representations to model 3D human shapes and appearances in a canonical space and then used deformation fields to deform the model into a posed space for rendering. These approaches achieve high-quality reconstruction results but require high memory and time consumption, as they typically require complex implicit representations, deformation algorithms, and volume rendering. One of these works InstantAvatar [26] is fast but suffers from artifacts in synthetic images. Our approach solves the problems of previous methods by combining parametric templates and implicit expressions to achieve fast and high-quality human reconstruction.

Accelerating Neural Rendering. Since the rendering speed of vanilla NeRF [35] is very slow, it takes several seconds to obtain an image and more time to train. Recent works [4, 16, 17, 28, 30, 31, 36, 36, 38, 43–45, 49] have been devoted to improving the speed of neural rendering. Plenoxels [16] proposed the utilization of a sparse volume, accompanied by density and spherical harmonic coefficients, for rendering purposes. TensoRF [4] decomposed the voxel grid into an aggregate of vector coefficients, aiming to reduce the size of the model for efficiency. Instant-NGP [36] introduced multi-resolution hash encoding to accomplish fast rendering. 3D-GS [28] represented each scene as a collection of scalable semi-transparent ellipsoids to achieve real-time rendering. These methods are mainly used for the reconstruction of static scenes. For dynamic scenes, FPO[45] presented a novel combination of NeRF, PlenOctree[49] representation, volumetric fusion, and Fourier transform to tackle efficient neural modeling and real-time rendering of dynamic scenes. InstantAvatar [26] applied hash encoding on 3d avatar reconstruction tasks for fast rendering. Such methods require high memory costs and suffer from artifacts. In this paper, we extend 3D-GS from static scenes to dynamic human scenes.

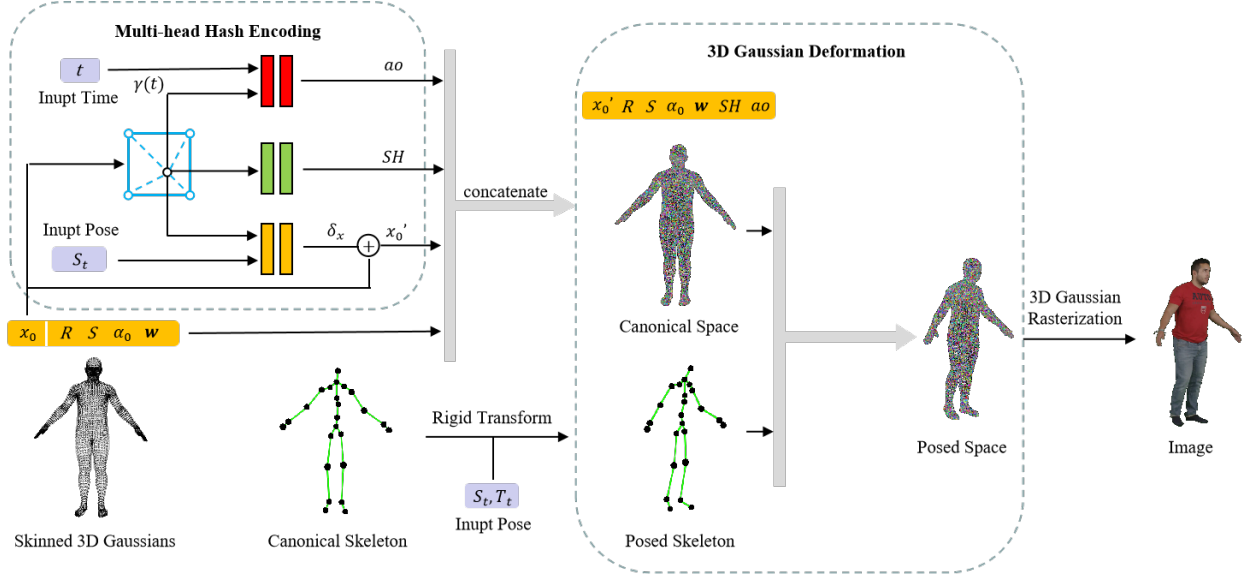


Figure 2: Overview. The proposed animatable 3D Gaussian consists of a set of skinned 3D Gaussians and a corresponding canonical skeleton. Each skinned 3D Gaussian contains center x_0 , rotation R , scale S , opacity α_0 , and skinning weights w . First, we sample spherical harmonic coefficients SH , vertex displacement δ_x , and ambient occlusion ao from the multi-head hash-encoded parameter field according to the center x_0 , where the multilayer perceptron for ao requires an additional frequency encoded time $\gamma(t)$ as input. Next, we concatenate the sampled parameters, the original parameters, and a shifted center x'_0 in canonical space. Finally, we deform 3D Gaussians to the posed space according to the input pose S_t, T_t and render them to the image using 3D Gaussian rasterization [28].

3 Preliminary

In this section, we briefly review the representation and pipeline of 3D Gaussian rasterization [28] in Sec. 3.1, and pose-based deformation in Sec. 3.2.

3.1 3D Gaussian Rasterization

Kerbl *et al.* [28] proposed to represent each scene as a collection of 3D Gaussians. Each 3D Gaussian P is defined as:

$$P = \{x_0, R, S, \alpha_0, SH\}, \quad (1)$$

where x_0 represents the geometric center of a 3D Gaussian distribution, R is a rotation matrix, S is a scaling matrix that scales the Gaussian in three dimensions, α_0 denotes the opacity of the center, and SH refers to a set of spherical harmonic coefficients used for modeling view-dependent color distribution following standard practice [16].

The opacity of position x in the vicinity of a 3D Gaussian P is defined as:

$$\alpha(x) = \alpha_0 e^{-\frac{1}{2}(x-x_0)^T \Sigma^{-1} (x-x_0)}, \quad (2)$$

where the covariance matrix Σ is decomposed into the rotation matrix R and the scaling matrix S :

$$\Sigma = RSS^T R^T. \quad (3)$$

Following the approach of Zwicker *et al.* [52], 3D Gaussians are projected to 2D image space as follows:

$$\Sigma' = PW\Sigma W^T P^T, \quad (4)$$

where W is a viewing transformation and P is the Jacobian of the affine approximation of the projective transformation.

Subsequently, the projected Gaussians are sorted based on their depths and rasterized to neighboring pixels according to Eq. (2). Each pixel receives a depth-sorted list of colors c_i and opacities α_i . The final pixel color C is computed by blending N ordered points overlapping the pixel:

$$C = \sum_{i \in N} c_i \alpha_i \prod_{j=1}^{i-1} (1 - \alpha_j). \quad (5)$$

3.2 Pose-guided Deformation

We define each frame within the video sequence as a posed space with a timestamp t and deform points from canonical space to posed space via linear blend skinning. We use a skinning weight field to model articulation. The skinning weight field [33] is defined as:

$$w(x_c) = \{w_1, \dots, w_{n_b}\}, \quad (6)$$

where n_b is the count of bones and x_c is a point in canonical space.

Target bone transformations $\mathbf{B}_t = \{B_1^t, \dots, B_{n_b}^t\}$ in frame t can be calculated from the input poses and the corresponding skeleton as follows:

$$S_t, J, T_t \mapsto \mathbf{B}_t, \quad (7)$$

where $S_t = \{\omega_1^t, \dots, \omega_{n_b}^t\}$ refers to the rotation Euler Angle of each joint in frame t (world rotation for ω_1^t and local rotation for the rest), T_t is the world translation in frame t , and $J = \{J_1, \dots, J_{n_b}\}$ is

the local position of each joint in canonical space. Please refer to the supplementary materials for the detailed calculation process.

Then we can deform points x_c in canonical space to the posed space via linear blend skinning:

$$x_t = \sum_{i=1}^{n_b} w_i B_i^t x_c, \quad (8)$$

where x_t refers to a point in frame t .

4 Method

Given a video sequence $\{I_t\}_{t=1}^T$ with one or more moving humans and their poses S_t, T_t , we reconstruct an animatable 3D Gaussian representation for each person in seconds. For multi-view video sequences, we reconstruct time-dependent ambient occlusion to achieve high-quality novel view synthesis.

In this section, we first introduce our animatable 3D Gaussian representation in Sec. 4.1. Then we deform 3D Gaussians from canonical space to posed space, as introduced in Sec. 3.2 and Sec. 4.2. Finally, we run 3D Gaussian rasterization (Sec. 3.1) to render an image for specific camera parameters. Moreover, we propose to build time-dependent ambient occlusion (Sec. 4.3) for multi-view, multi-person, and wide-range motion tasks, which enables our algorithm to fit dynamic shadows caused by occlusion. The pipeline of the proposed method is illustrated in Fig. 2.

4.1 Animatable 3D Gaussian in Canonical Space

3D Gaussians with Skeleton. We bind 3D Gaussians to a corresponding skeleton to enable the linear skinning algorithm in Eq. (8). The proposed animatable 3D Gaussian representation consists of a set of skinned 3D Gaussians and a corresponding skeleton \mathbf{J} mentioned in Eq. (7). The skinned 3D Gaussian P_{skin} is adapted from the static 3D Gaussian P in Eq. (1) and defined as follows:

$$P_{skin} = \{x_0, R, S, \alpha_0, SH, \mathbf{w}, \delta_x\}, \quad (9)$$

where \mathbf{w} is the skinning weights, and δ_x is the vertex displacement.

Directly optimizing the skinning weights from random initialization is a significant challenge. Instead, we treat the skinning weights as a strong prior for a generic human body model unrelated to any specific human shape. In practice, we initialize the skinning weights and positions of Gaussian points using a standard skinned model as discussed in Sec. 4.4. During optimization, the skinning weights \mathbf{w} are kept fixed, while the vertex displacement δ_x and skeleton \mathbf{J} are optimized to capture the shape and motion of an individual accurately. We shift the Gaussian center x_0 before implementing pose-based deformation in Eq. (8):

$$x_0' = x_0 + \delta_x. \quad (10)$$

Multi-Head Hash-encoder. We note that using per-vertex colors performs poorly in deformable dynamic scenes [28]. Since the deformation of Gaussians from canonical space to posed space is initially uncertain, it needs more samples and iterations to reach convergence. Moreover, rendering based on 3D Gaussian rasterization can only backpropagate the gradient to a finite number of Gaussians in a single iteration, which leads to a slow or even divergent optimization process for dynamic scenes. To address this issue, we suggest sampling spherical harmonic coefficients SH for each vertex from a continuous parameter field, which is able to affect

all neighboring Gaussians in a single optimization. Similarly, using unconstrained per-vertex displacement can easily cause the optimization process to diverge in dynamic scenes. Therefore, we also model a parameter field for vertex displacement. For the remaining parameters in Eq. (9), we store them in each point to preserve the ability of the 3D Gaussian to fit different shapes. We define the parameter fields as follows:

$$x_0 \mapsto SH. \quad (11)$$

In order to acquire pose-dependent deformation, we add pose S_t as an additional input for vertex displacement:

$$x_0, S_t \mapsto \delta_x. \quad (12)$$

Since our animatable 3D Gaussian representation is initialized by a standard human body model, the centers of 3D Gaussians are uniformly distributed near the human surface. We only need to sample at fixed positions near the surface of the human body in the parameter fields. This allows for significant compression of the hash table for the hash encoding [36]. Thus, we choose the hash encoding to model our parameter field to reduce the time and storage consumption.

Optionally, we provide UV-encoded spherical harmonic coefficients, allowing fast processing of custom human models with UV coordinate mappings. UV encoding potentially achieves higher reconstruction quality compared to hash encoding. The UV mapping for spherical harmonic coefficients SH is defined as follows:

$$u, v \mapsto SH, \quad (13)$$

where u, v is the UV coordinate of a 3D Gaussian.

4.2 3D Gaussian Deformation

We use poses to guide the deformation of 3D Gaussians illustrated in Fig. 3. We introduce pose-based deformation which transforms the point position from the canonical space to the posed space in Sec. 3.2. For 3D Gaussians, we also need to deform their orientation to achieve a consistent anisotropic Gaussian distribution at different poses. Using the same orientation in different poses causes the 3D Gaussian to degenerate into Gaussian spheres. Same as Eq. (8), we apply the linear blend skinning to the rotation R of 3D Gaussians as follows:

$$R_t = \sum_{i=1}^{n_b} w_i B_i^t R_c, \quad (14)$$

where R_c is the rotation in canonical space and R_t is the rotation in posed space in frame t .

The view direction for the computation of color based on spherical harmonics should be deformed to canonical space, in order to achieve consistent anisotropic colors. Hence, we apply the inverse transformation of the linear blend skinning to the view direction:

$$d_c = \left(\sum_{i=1}^{n_b} w_i B_i^t \right)^{-1} d_t, \quad (15)$$

where d_c is the direction in canonical space and d_t is the direction in posed space in frame t .

We implement the mentioned transformations by extending the 3D Gaussian rasterizer [28] and explicitly derive the gradients for all parameters. This makes the time overhead for the pose-based deformation of 3D Gaussians almost negligible.

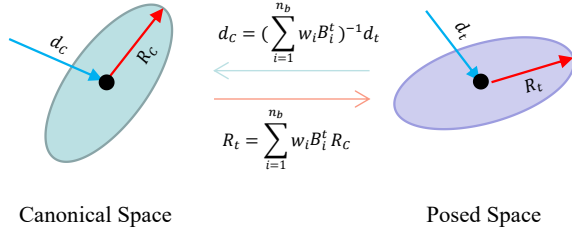


Figure 3: 3D Gaussian Deformation. The rotation R_c of 3D Gaussian in canonical space is deformed into the posed space using Eq. (14), while view direction d_t is implemented the inverse transformation in Eq. (15).

4.3 Time-dependent Ambient Occlusion

We propose a time-dependent ambient occlusion module to address the issue of dynamic shadows in specific scenes. We additionally model an ambient occlusion factor $ao \in [0, 1]$ on top of the skinned 3D Gaussian in Eq. (9) as follows:

$$P'_{skin} = \{x_0, R, S, \alpha_0, SH, \mathbf{w}, \delta_x, ao\}. \quad (16)$$

We calculate the color after considering the ambient occlusion for each individual Gaussian as follows:

$$c = ao \cdot Y(SH, d_c), \quad (17)$$

where Y refers to the spherical harmonics.

As discussed in Sec. 4.1, we also employ hash encoding for the ambient occlusion ao , since shadows should be continuously modeled in space. Furthermore, we introduce an additional input of the positional encoding [35] of time t in the MLP module of the hashing encoding [36] in order to capture time-dependent ambient occlusion. The parameter field for ambient occlusion is defined as:

$$x_0, \gamma(t) \mapsto ao, \quad (18)$$

where function $\gamma(\cdot)$ refers to the positional encoding used in NeRF [35].

At the beginning of training, we use a fixed ambient occlusion to allow the model to learn time-independent spherical harmonic coefficients. We start optimizing the ambient occlusion after the color stabilizes.

4.4 Optimization Details

Animatable 3D Gaussian Initialization. The initialization of the 3D Gaussian has a significant impact on the quality of optimization results. Improper initialization can even lead to divergence in the optimization process. For static 3D Gaussians [28], the Structure-from-Motion (SfM [41]) method is used to obtain the initial 3D Gaussian point cloud, which provides a very good and dense initialization.

However, for dynamic scenes, obtaining an initial point cloud using SfM is a huge challenge. Therefore, we use a standard skinned model to initialize our deformable 3D Gaussian representation. This standard skinned model should include a set of positions and skinning weights \mathbf{w} , and a skeleton \mathbf{J} corresponding to the input poses. We recommend upsampling the vertices of the input model to around 100,000 to achieve high reconstruction quality. Specifically, for the SMPL model [33], we randomly sample K additional points

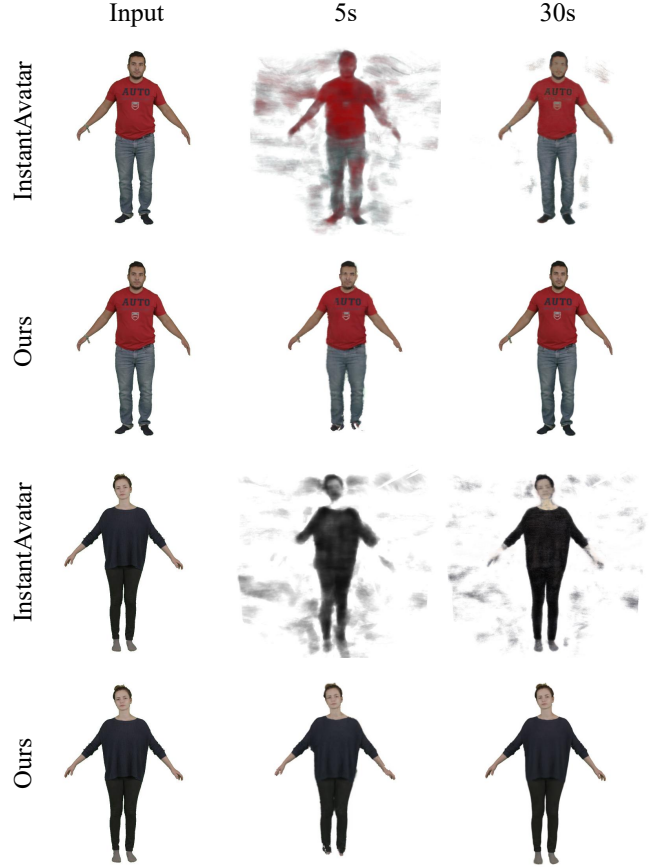


Figure 4: Qualitative Results on PeopleSnapshot [1] Dataset. We show the image quality of our method and InstantAvatar [26] at 5s and 30s training time. Compared to InstantAvatar, our method achieves higher reconstruction quality and a significant reduction in artifacts.

(we set $K=20$ based on experimental results) within the neighborhood of each vertex and directly copy their skinning parameters to get a model of around 140,000 points.

Loss Function. The proposed animatable 3D Gaussian representation is capable of accurately fitting dynamic scenes containing moving humans, thus eliminating the need for additional regularization losses. We directly employ a combination of \mathcal{L}_1 and D-SSIM term:

$$\mathcal{L} = (1 - \lambda)\mathcal{L}_1 + \lambda\mathcal{L}_{D-SSIM}, \quad (19)$$

where we use $\lambda = 0.2$ following the best practices of the static 3D Gaussian [28].

5 Experiments

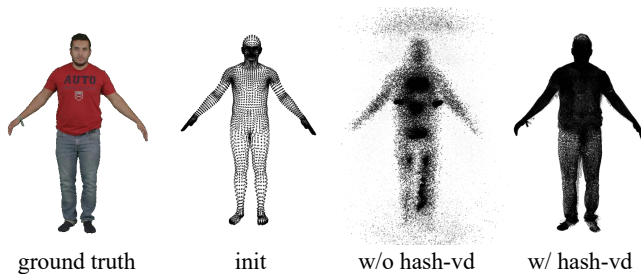
We evaluate the speed and quality (PSNR, SSIM [46], and LPIPS [51]) of our method on monocular scenes (Sec. 5.1) and multi-view scenes (Sec. 5.2). Comparative experiments with state-of-the-art methods [5, 26] show the superiority of our method. In addition, we

Table 1: Comparison on PeopleSnapshot [1] Dataset. We compare our results with InstantAvatar [26] at 5s and 30s training time and provide Anim-NeRF’s results [5] at 5-minute training time.

	training↓	male-3-casual			male-4-casual			female-3-casual			female-4-casual		
		PSNR↑	SSIM↑	LPIPS↓	PSNR↑	SSIM↑	LPIPS↓	PSNR↑	SSIM↑	LPIPS↓	PSNR↑	SSIM↑	LPIPS↓
Anim-NeRF [5]	5m	23.17	0.9266	0.0784	22.30	0.9235	0.0911	22.37	0.9311	0.0784	23.18	0.9292	0.0687
InstantAvatar [26]	30s	26.56	0.9301	0.1190	26.10	0.9289	0.1397	22.37	0.8427	0.2687	26.32	0.9281	0.1333
Ours	30s	29.06	0.9704	0.0264	26.16	0.9554	0.0491	24.59	0.9535	0.0399	27.26	0.9634	0.0281
InstantAvatar [26]	5s	17.30	0.7980	0.3473	16.44	0.7960	0.3508	17.22	0.8185	0.3262	14.91	0.7606	0.3878
Ours	5s	22.84	0.9395	0.0632	18.88	0.9103	0.1175	20.51	0.9301	0.0764	20.63	0.9246	0.0737

Table 2: Comparison on ZJU-MoCap [37]. Compared with competitive baselines [26, 37, 50], our approach achieves the best on SSIM and the best or second best on two other metrics. Cell color indicates **best and **second best**.**

	training↓	FPS↑	377			386			387			392			394		
			PSNR↑	SSIM↑	LPIPS↓	PSNR↑	SSIM↑	LPIPS↓	PSNR↑	SSIM↑	LPIPS↓	PSNR↑	SSIM↑	LPIPS↓	PSNR↑	SSIM↑	LPIPS↓
NeuralBody [37]	12h	2	29.11	0.9674	0.0410	30.54	0.9678	0.0464	27.00	0.9518	0.0594	30.10	0.9642	0.0533	29.10	0.9593	0.0546
MonoHuman [50]	4d	0.1	29.12	0.9727	0.0265	32.94	0.9695	0.0361	27.93	0.9601	0.0417	29.50	0.9635	0.0395	29.15	0.9595	0.0381
InstantAvatar [26]	120s	8	29.92	0.9676	0.0600	32.57	0.9605	0.0864	28.41	0.9541	0.0861	30.98	0.9677	0.0595	30.32	0.9617	0.0656
Ours	60s	120	30.51	0.9761	0.0332	32.65	0.9733	0.0396	28.04	0.9618	0.0526	30.77	0.9699	0.0473	29.89	0.9626	0.0493

**Figure 5: Ablation Study of Hash-Encoded Vertex Displacement. Without hash-encoded vertex displacement (w/o hash-vd), the centers of 3D Gaussians may diverge during the optimization process, while our hash-encoded vertex displacement (w/ hash-vd) converges to the ground truth shape.****Table 3: Ablation Study on PeopleSnapshot [1] Dataset. We respectively remove the hash-encoded spherical harmonic coefficients (hash-SH), hash-encoded vertex displacement (hash-vd), and joint optimization (J-optimize) from our method, and compare their results with our full method.**

	PSNR↑	SSIM↑	LPIPS↓
w/o hash-SH	25.38	0.9478	0.0504
w/o hash-vd	22.08	0.8994	0.1678
w/o J-optimize	21.45	0.9311	0.0781
ours	26.77	0.9607	0.0359

provide extensive ablation studies of our methods. In all experiments, we evaluate our approach on a single RTX 3090 and do not use any predicted body parameters but a generic template.

5.1 Monocular Scenes

We use the PeopleSnapshot [1] and ZJU-MoCap [37] dataset to evaluate the performance of our method in single-human, monocular scenes.

PeopleSnapshot. Following the previous approach [26], we downsample the images to 540×540 resolution and use the SMPL [33] model for initialization. Since this dataset does not contain time-stamps and drastic shading variations, we do not use the time-dependent ambient occlusion module.

We provide quantitative comparisons in Tab. 1 and visual comparisons in Fig. 4. Compared to InstantAvatar [26] and Anim-NeRF [5], our method achieves higher reconstruction quality in a shorter training time (5s and 30s). As shown in Fig. 4, our method solves the problem of artifacts that have occurred in the previous methods. Moreover, our method achieves the fastest training and rendering speed. For 540×540 resolution images, we reach a training speed of 50 FPS and a rendering speed of 170 FPS.

ZJU-MoCap. We pick 5 sequences (377, 386, 387, 392, 394) in the ZJU-MoCap dataset to evaluate our method and select camera 1 as the train set and the remaining 22 cameras as the test set. In keeping with baselines [26, 37, 50], we downsample the images to 512×512 resolution.

Tab. 2 shows that our method is superior to other baseline methods on SSIM, and also achieves best or second best on PSNR and LPIPS. In comparison with NeuralBody [37] and MonoHuman [50], our approach achieves a $240 \times$ faster speed in training time and a $60 \times$ faster speed in rendering speed. In comparison to the main baseline InstantAvatar [26], our approach achieved a $2 \times$ faster speed in training time and a $15 \times$ faster speed in rendering speed.

Ablation Study. We performed ablation experiments on the PeopleSnapshot dataset. Tab. 3 quantitatively illustrates that our proposed hash-encoded spherical harmonic coefficients, hash-encoded



Figure 6: Novel View Synthesis Results on Single-Human Scenes of GalaBasketball Dataset. We show the novel view synthesis quality of our method (with hash-encoded spherical harmonic coefficients) and InstantAvatar [26].

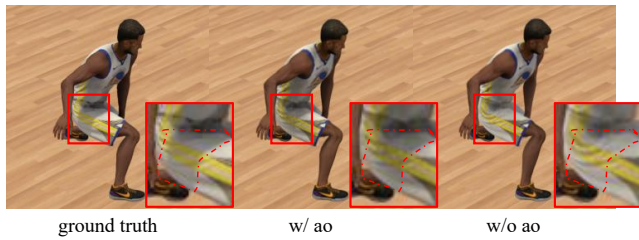


Figure 7: Ablation Study of Time-dependent Ambient Occlusion. Dynamic shadows can not be reconstructed without time-dependent ambient occlusion (w/o ao), resulting in low novel view synthesis quality. Our proposed time-dependent ambient occlusion is able to fit dynamic shadows and synthesize high-quality novel view shadows.

vertex displacement, and joint optimization, can improve the quality of the reconstruction in a short period of training time (30s). We also visualize the point cloud optimization results in Fig. 5 to show the effect of hash-encoded vertex displacement.

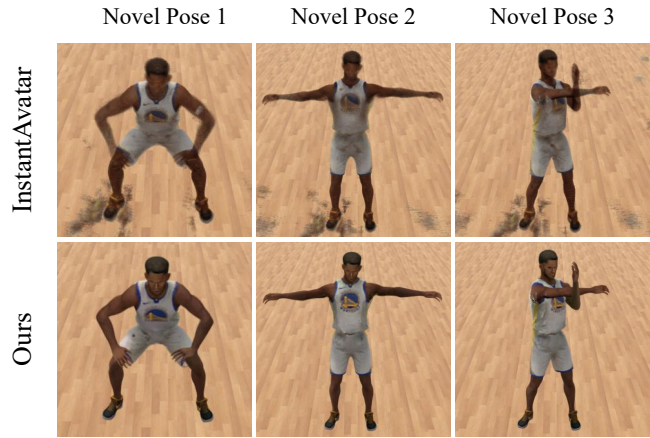


Figure 8: Novel Pose Synthesis Results on Single-Human Scenes of GalaBasketball Dataset. We compare the novel pose synthesis quality of our method (without time-dependent ambient occlusion) with InstantAvatar [26].

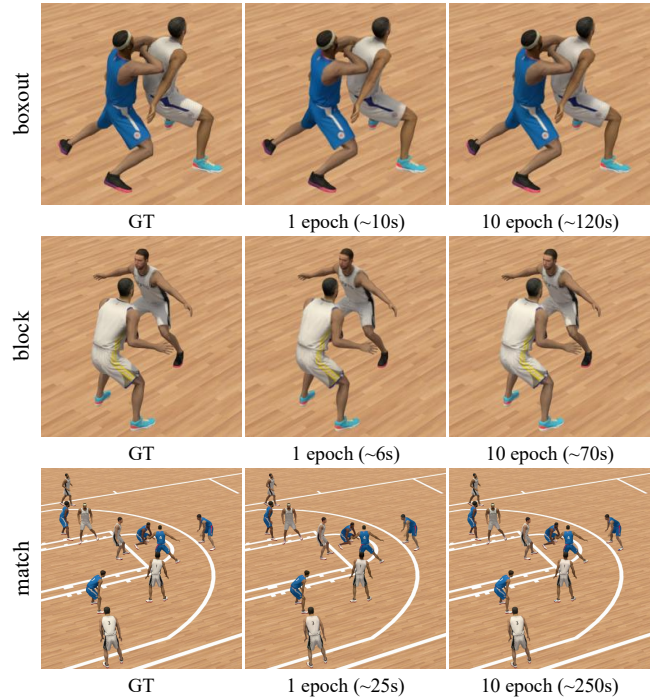


Figure 9: Novel View Synthesis Results on Multi-Human Scenes. We provide novel view synthesis results of our method trained for 1 epoch and 10 epochs on multi-human scenes. Trained for only one epoch, our method achieves comparable quality to the ground truth (GT). Longer training allows our model to fit higher-quality dynamic shadows.

Table 4: Comparison on Single-Human Scenes of GalaBasketball Dataset. We provide our novel view synthesis results under different settings, including without time-dependent ambient occlusion (w/o ao) and our full method, all trained for the 10 epochs (around 1 minute). We compare them with InstantAvatar [26] and raw 3D-GS [28].

	training↓	idle			dribble			shot			turn		
		PSNR↑	SSIM↑	LPIPS↓	PSNR↑	SSIM↑	LPIPS↓	PSNR↑	SSIM↑	LPIPS↓	PSNR↑	SSIM↑	LPIPS↓
InstantAvatar [26]	5m	29.86	0.9607	0.0575	27.25	0.9435	0.0903	29.22	0.9461	0.0709	32.20	0.9705	0.0371
3D-GS [28]	60s	37.38	0.9941	0.0042	36.53	0.9909	0.0059	37.07	0.9908	0.0067	35.74	0.9919	0.0071
Ours: w/o ao	50s	37.45	0.9943	0.0046	36.87	0.9915	0.0059	37.47	0.9921	0.0068	36.77	0.9927	0.0062
Ours	60s	40.75	0.9964	0.0029	38.53	0.9935	0.0042	39.44	0.9936	0.0049	39.74	0.9953	0.0038

5.2 Multi-View Scenes

There are few pose and shadow changes in the PeopleSnapshot [1] dataset. In order to demonstrate the reconstruction performance of the proposed method in scenes containing complex motions and dynamic shadows, we create a dataset called GalaBasketball, which is synthesized from several player models with different shapes and appearances. The GalaBasketball dataset consists of four single-human and three multi-human scenes, providing six uniformly surrounded cameras as a training set and one camera as a test set. For the single-human scenes, we provide an additional set of actions to evaluate the novel pose synthesis capability. Moreover, We provide a standard skinned model corresponding to the GalaBasketball dataset for initialization, which does not resemble any of the players in the dataset in terms of geometry and appearance.

Novel View Synthesis. As shown in Tab. 4 and Fig. 6, we evaluate the ability of our method and InstantAvatar [26] to synthesize novel views on the single-human scenes of GalaBasketball. Compared with InstantAvatar [26], our approach under any setting achieves a higher-quality synthesis of novel views in a shorter training time and significantly eliminates artifacts. This proves that our animatable 3D Gaussian representation can be trained under complex motion variations and obtain high-quality human avatars. In contrast, InstantAvatar suffers from artifacts and achieves low synthesis quality, because skin weights fail to converge to the ground truth under complex motion variations.

Ablation Study. We also provide the result of raw 3D-GS [28] and our result without ambient occlusion in Tab. 4. The comparison results between 3D-GS and our full methods demonstrate the validity of our proposed Animatable 3D Gaussian representation. The ablation experiment of ambient occlusion shows that the time-dependent ambient occlusion helps our method achieve higher novel view synthesis quality, which fits time-dependent shadow changes as shown in Fig. 7.

Novel Pose Synthesis. We render the images using the other set of actions different from the training set and compare our novel pose synthesis results with InstantAvatar in Fig. 8. Since the novel pose synthesis task does not have a timestamp, we do not use the time-dependent ambient occlusion. The result shows that our reconstructed human avatar achieves high synthesis quality in novel poses, while InstantAvatar still suffers from artifacts.

Multi-Human Scenes. We extend our method to multi-human scenes by rendering multiple human avatars simultaneously on a single RTX 3090, while the existing methods [5, 26] can not be extended to multi-human scenes due to the limitations of implementation and memory. Fig. 9 shows the high-quality novel view synthesis results of our method in the multi-human scenes of GalaBasketball, including two double-human scenes and a 5v5 scene. The comparison results between 1 epoch and 10 epochs show that our method can learn the time-dependent dynamic shadows through training. Our method achieves a training speed of 40 FPS and a rendering speed of 110 FPS on double-human scenes (512×512 resolution). On the 5v5 scene (1920×1080 resolution), our method reaches a training speed of 10 FPS and a rendering speed of 40 FPS.

6 Conclusion

We propose a method for high-quality human reconstruction in seconds. The reconstructed human avatar can be used for real-time novel view synthesis and novel pose synthesis. Our method consists of the Animatable 3D Gaussian representation in canonical space and pose-based 3D Gaussian deformation, which extends 3D Gaussian [28] to deformable humans. Our proposed time-dependent ambient occlusion achieves high-quality reconstruction results in scenes containing complex motions and dynamic shadows. Compared to the state-of-the-art methods [5, 26], our method takes less training time, renders faster, and yields better reconstruction results. Moreover, our approach can be easily extended to multi-human scenes.

Limitations and Future Work. To implement optional modules, our approach uses multiple MLPs. However, in specific tasks, multiple MLPs can be merged into one to further reduce training consumption. Due to the complexity of the dynamic scenes, we do not add or remove Gaussian points during the training process, which leads to the quality of the reconstruction greatly affected by the number of initialized points, and reduces the reconstruction quality in the high-frequency region. Considering the training speed, our method does not optimize pose which fails in scenes with inaccurate poses.

Acknowledgments

This research was funded through the National Key Research and Development Program of China (Project No. 2022YFB36066), partly by the Shenzhen Science and Technology Project under Grant (JCYJ20220818101001004).

References

- [1] Thiemo Alldieck, Marcus Magnor, Weipeng Xu, Christian Theobalt, and Gerard Pons-Moll. 2018. Detailed human avatars from monocular video. In *2018 International Conference on 3D Vision (3DV)*. IEEE, 98–109.
- [2] Thiemo Alldieck, Marcus Magnor, Weipeng Xu, Christian Theobalt, and Gerard Pons-Moll. 2018. Video based reconstruction of 3d people models. In *Proceedings of the IEEE Conference on Computer Vision and Pattern Recognition*. 8387–8397.
- [3] Alexander Bergman, Petr Kellnhofer, Wang Yifan, Eric Chan, David Lindell, and Gordon Wetzstein. 2022. Generative neural articulated radiance fields. *Advances in Neural Information Processing Systems* 35 (2022), 19900–19916.
- [4] Anpei Chen, Zexiang Xu, Andreas Geiger, Jingyi Yu, and Hao Su. 2022. Tensorf: Tensorial radiance fields. In *European Conference on Computer Vision*. Springer, 333–350.
- [5] Jianchuan Chen, Ying Zhang, Di Kang, Xuefei Zhe, Linchao Bao, Xu Jia, and Huchuan Lu. 2021. Animatable neural radiance fields from monocular rgb videos. *arXiv preprint arXiv:2106.13629* (2021).
- [6] Xu Chen, Tianjian Jiang, Jie Song, Jinlong Yang, Michael J Black, Andreas Geiger, and Otmar Hilliges. 2022. gdna: Towards generative detailed neural avatars. In *Proceedings of the IEEE/CVF Conference on Computer Vision and Pattern Recognition*. 20427–20437.
- [7] Xu Chen, Yufeng Zheng, Michael J Black, Otmar Hilliges, and Andreas Geiger. 2021. Snarf: Differentiable forward skinning for animating non-rigid neural implicit shapes. In *Proceedings of the IEEE/CVF International Conference on Computer Vision*. 11594–11604.
- [8] Julian Chibane, Thiemo Alldieck, and Gerard Pons-Moll. 2020. Implicit functions in feature space for 3d shape reconstruction and completion. In *Proceedings of the IEEE/CVF conference on computer vision and pattern recognition*. 6970–6981.
- [9] Alvaro Collet, Ming Chuang, Pat Sweeney, Don Gillett, Dennis Evseev, David Calabrese, Hugues Hoppe, Adam Kirk, and Steve Sullivan. 2015. High-quality streamable free-viewpoint video. *ACM Transactions on Graphics (ToG)* 34, 4 (2015), 1–13.
- [10] Enric Corona, Albert Pumarola, Guillem Alenya, Gerard Pons-Moll, and Francesc Moreno-Noguer. 2021. Smplify: Topology-aware generative model for clothed people. In *Proceedings of the IEEE/CVF conference on computer vision and pattern recognition*. 11875–11885.
- [11] Paul Debevec, Tim Hawkins, Chris Tchou, Haarm-Pieter Duiker, Westley Sarokin, and Mark Sagar. 2000. Acquiring the reflectance field of a human face. In *Proceedings of the 27th annual conference on Computer graphics and interactive techniques*. 145–156.
- [12] Paul E Debevec, Camillo J Taylor, and Jitendra Malik. 2023. Modeling and rendering architecture from photographs: A hybrid geometry-and image-based approach. In *Seminal Graphics Papers: Pushing the Boundaries, Volume 2*. 465–474.
- [13] Zijian Dong, Chen Guo, Jie Song, Xu Chen, Andreas Geiger, and Otmar Hilliges. 2022. PINA: Learning a personalized implicit neural avatar from a single RGB-D video sequence. In *Proceedings of the IEEE/CVF Conference on Computer Vision and Pattern Recognition*. 20470–20480.
- [14] Mingsong Dou, Sameh Khamis, Yury Degtyarev, Philip Davidson, Sean Ryan Fanello, Adarsh Kowdle, Sergio Orts Escolano, Christoph Rhemann, David Kim, Jonathan Taylor, et al. 2016. Fusion4d: Real-time performance capture of challenging scenes. *ACM Transactions on Graphics (ToG)* 35, 4 (2016), 1–13.
- [15] Yao Feng, Jinlong Yang, Marc Pollefeys, Michael J Black, and Timo Bolkart. 2022. Capturing and animation of body and clothing from monocular video. In *SIGGRAPH Asia 2022 Conference Papers*. 1–9.
- [16] Sara Fridovich-Keil, Alex Yu, Matthew Tancik, Qinlong Chen, Benjamin Recht, and Angjoo Kanazawa. 2022. Plenoxels: Radiance fields without neural networks. In *Proceedings of the IEEE/CVF Conference on Computer Vision and Pattern Recognition*. 5501–5510.
- [17] Stephan J Garbin, Marek Kowalski, Matthew Johnson, Jamie Shotton, and Julien Valentin. 2021. Fastnerf: High-fidelity neural rendering at 200fps. In *Proceedings of the IEEE/CVF International Conference on Computer Vision*. 14346–14355.
- [18] Chen Guo, Xu Chen, Jie Song, and Otmar Hilliges. 2021. Human performance capture from monocular video in the wild. In *2021 International Conference on 3D Vision (3DV)*. IEEE, 889–898.
- [19] Kaiwen Guo, Peter Lincoln, Philip Davidson, Jay Busch, Xueming Yu, Matt Whalen, Geoff Harvey, Sergio Orts-Escolano, Rohit Pandey, Jason Dourgarian, et al. 2019. The rightlights: Volumetric performance capture of humans with realistic relighting. *ACM Transactions on Graphics (ToG)* 38, 6 (2019), 1–19.
- [20] Marc Habermann, Weipeng Xu, Michael Zollhoefer, Gerard Pons-Moll, and Christian Theobalt. 2019. Livecap: Real-time human performance capture from monocular video. *ACM Transactions On Graphics (TOG)* 38, 2 (2019), 1–17.
- [21] Marc Habermann, Weipeng Xu, Michael Zollhoefer, Gerard Pons-Moll, and Christian Theobalt. 2020. Deepcap: Monocular human performance capture using weak supervision. In *Proceedings of the IEEE/CVF Conference on Computer Vision and Pattern Recognition*. 5052–5063.
- [22] Tong He, John Collomosse, Hailin Jin, and Stefano Soatto. 2020. Geo-pifu: Geometry and pixel aligned implicit functions for single-view human reconstruction. *Advances in Neural Information Processing Systems* 33 (2020), 9276–9287.
- [23] Tong He, Yuanlu Xu, Shunsuke Saito, Stefano Soatto, and Tony Tung. 2021. Arch++: Animation-ready clothed human reconstruction revisited. In *Proceedings of the IEEE/CVF international conference on computer vision*. 11046–11056.
- [24] Zeng Huang, Yuanlu Xu, Christoph Lassner, Hao Li, and Tony Tung. 2020. Arch: Animatable reconstruction of clothed humans. In *Proceedings of the IEEE/CVF Conference on Computer Vision and Pattern Recognition*. 3093–3102.
- [25] Boyi Jiang, Yang Hong, Hujun Bao, and Juyong Zhang. 2022. Selfrecon: Self reconstruction your digital avatar from monocular video. In *Proceedings of the IEEE/CVF Conference on Computer Vision and Pattern Recognition*. 5605–5615.
- [26] Tianjian Jiang, Xu Chen, Jie Song, and Otmar Hilliges. 2023. Instantavatar: Learning avatars from monocular video in 60 seconds. In *Proceedings of the IEEE/CVF Conference on Computer Vision and Pattern Recognition*. 16922–16932.
- [27] Wei Jiang, Kwang Moo Yi, Golnoosh Samei, Oncel Tuzel, and Anurag Ranjan. 2022. Neuman: Neural human radiance field from a single video. In *European Conference on Computer Vision*. Springer, 402–418.
- [28] Bernhard Kerbl, Georgios Kopanas, Thomas Leimkühler, and George Drettakis. 2023. 3d gaussian splatting for real-time radiance field rendering. *ACM Transactions on Graphics (ToG)* 42, 4 (2023), 1–14.
- [29] Ruilong Li, Julian Tanke, Minh Vo, Michael Zollhöfer, Jürgen Gall, Angjoo Kanazawa, and Christoph Lassner. 2022. Tava: Template-free animatable volumetric actors. In *European Conference on Computer Vision*. Springer, 419–436.
- [30] David B Lindell, Julien NP Martel, and Gordon Wetzstein. 2021. Autoint: Automatic integration for fast neural volume rendering. In *Proceedings of the IEEE/CVF Conference on Computer Vision and Pattern Recognition*. 14556–14565.
- [31] Lingjie Liu, Jiatao Gu, Kyaw Zaw Lin, Tat-Seng Chua, and Christian Theobalt. 2020. Neural sparse voxel fields. *Advances in Neural Information Processing Systems* 33 (2020), 15651–15663.
- [32] Lingjie Liu, Marc Habermann, Viktor Rudnev, Kripasindhu Sarkar, Jiatao Gu, and Christian Theobalt. 2021. Neural actor: Neural free-view synthesis of human actors with pose control. *ACM transactions on graphics (TOG)* 40, 6 (2021), 1–16.
- [33] Matthew Loper, Naureen Mahmood, Javier Romero, Gerard Pons-Moll, and Michael J Black. 2023. SMPL: A skinned multi-person linear model. In *Seminal Graphics Papers: Pushing the Boundaries, Volume 2*. 851–866.
- [34] Marko Mihajlovic, Yan Zhang, Michael J Black, and Siyu Tang. 2021. LEAP: Learning articulated occupancy of people. In *Proceedings of the IEEE/CVF Conference on Computer Vision and Pattern Recognition*. 10461–10471.
- [35] Ben Mildenhall, Pratul P Srinivasan, Matthew Tancik, Jonathan T Barron, Ravi Ramamoorthi, and Ren Ng. 2021. Nerf: Representing scenes as neural radiance fields for view synthesis. *Commun. ACM* 65, 1 (2021), 99–106.
- [36] Thomas Müller, Alex Evans, Christoph Schied, and Alexander Keller. 2022. Instant neural graphics primitives with a multi-resolution hash encoding. *ACM Transactions on Graphics (ToG)* 41, 4 (2022), 1–15.
- [37] Sida Peng, Yuanqing Zhang, Yinghao Xu, Qianqian Wang, Qing Shuai, Hujun Bao, and Xiaowei Zhou. 2021. Neural body: Implicit neural representations with structured latent codes for novel view synthesis of dynamic humans. In *Proceedings of the IEEE/CVF Conference on Computer Vision and Pattern Recognition*. 9054–9063.
- [38] Christian Reiser, Songyou Peng, Yiyi Liao, and Andreas Geiger. 2021. Kilonerf: Speeding up neural radiance fields with thousands of tiny mlps. In *Proceedings of the IEEE/CVF International Conference on Computer Vision*. 14335–14345.
- [39] Shunsuke Saito, Zeng Huang, Ryota Natsume, Shigeo Morishima, Angjoo Kanazawa, and Hao Li. 2019. Pifu: Pixel-aligned implicit function for high-resolution clothed human digitization. In *Proceedings of the IEEE/CVF international conference on computer vision*. 2304–2314.
- [40] Shunsuke Saito, Tomas Simon, Jason Saragih, and Hanbyul Joo. 2020. Pifuhd: Multi-level pixel-aligned implicit function for high-resolution 3d human digitization. In *Proceedings of the IEEE/CVF Conference on Computer Vision and Pattern Recognition*. 84–93.
- [41] Johannes L Schonberger and Jan-Michael Frahm. 2016. Structure-from-motion revisited. In *Proceedings of the IEEE conference on computer vision and pattern recognition*. 4104–4113.
- [42] Zhuo Su, Lan Xu, Zerong Zheng, Tao Yu, Yebin Liu, and Lu Fang. 2020. Robust-fusion: Human volumetric capture with data-driven visual cues using a rgbd camera. In *Computer Vision—ECCV 2020: 16th European Conference, Glasgow, UK, August 23–28, 2020, Proceedings, Part IV 16*. Springer, 246–264.
- [43] Cheng Sun, Min Sun, and Hwann-Tzong Chen. 2022. Direct voxel grid optimization: Super-fast convergence for radiance fields reconstruction. In *Proceedings of the IEEE/CVF Conference on Computer Vision and Pattern Recognition*. 5459–5469.

- [44] Angtian Wang, Peng Wang, Jian Sun, Adam Kortylewski, and Alan Yuille. 2022. VoGE: a differentiable volume renderer using gaussian ellipsoids for analysis-by-synthesis. In *The Eleventh International Conference on Learning Representations*.
- [45] Liao Wang, Jiakai Zhang, Xinhang Liu, Fuqiang Zhao, Yanshun Zhang, Yingliang Zhang, Minye Wu, Jingyi Yu, and Lan Xu. 2022. Fourier plenotrees for dynamic radiance field rendering in real-time. In *Proceedings of the IEEE/CVF Conference on Computer Vision and Pattern Recognition*. 13524–13534.
- [46] Zhou Wang, Alan C Bovik, Hamid R Sheikh, and Eero P Simoncelli. 2004. Image quality assessment: from error visibility to structural similarity. *IEEE transactions on image processing* 13, 4 (2004), 600–612.
- [47] Donglai Xiang, Fabian Prada, Chenglei Wu, and Jessica Hodgins. 2020. Monoclothcap: Towards temporally coherent clothing capture from monocular rgb video. In *2020 International Conference on 3D Vision (3DV)*. IEEE, 322–332.
- [48] Weipeng Xu, Avishek Chatterjee, Michael Zollhöfer, Helge Rhodin, Dushyant Mehta, Hans-Peter Seidel, and Christian Theobalt. 2018. Monoperfcap: Human performance capture from monocular video. *ACM Transactions on Graphics (ToG)* 37, 2 (2018), 1–15.
- [49] Alex Yu, Ruilong Li, Matthew Tancik, Hao Li, Ren Ng, and Angjoo Kanazawa. 2021. Plenotrees for real-time rendering of neural radiance fields. In *Proceedings of the IEEE/CVF International Conference on Computer Vision*. 5752–5761.
- [50] Zhengming Yu, Wei Cheng, Xian Liu, Wayne Wu, and Kwan-Yee Lin. 2023. MonoHuman: Animatable Human Neural Field from Monocular Video. In *Proceedings of the IEEE/CVF Conference on Computer Vision and Pattern Recognition*. 16943–16953.
- [51] Richard Zhang, Phillip Isola, Alexei A Efros, Eli Shechtman, and Oliver Wang. 2018. The unreasonable effectiveness of deep features as a perceptual metric. In *Proceedings of the IEEE conference on computer vision and pattern recognition*. 586–595.
- [52] Matthias Zwicker, Hanspeter Pfister, Jeroen Van Baar, and Markus Gross. 2001. EWA volume splatting. In *Proceedings Visualization, 2001. VIS'01*. IEEE, 29–538.

Animatable 3D Gaussian: Fast and High-Quality Reconstruction of Multiple Human Avatars

A Overview

In the supplementary material, we introduce the calculation process of bone transformation and discuss the feasibility of optimizing the joint positions in canonical space. Furthermore, we provide more visualization results. We encourage the reader to watch the video for our high-quality results.

B Calculation of Bone Transformation

We introduce bone transformation in Sec. 3.2. In this section, we provide the detailed calculation process of Eq. 7 and discuss the need to optimize the joint positions in canonical space.

We combine posed translation T_t and rotation angle ω_1^t to obtain the posed transformation $B_{posed,1}^t$ of the root joint:

$$B_{posed,1}^t = \begin{bmatrix} \mathbf{R}(\omega_1^t) & T_t \\ 0 & 1 \end{bmatrix}, \quad (20)$$

where $\mathbf{R}(\cdot)$ denotes a function that converts the Euler angle to a rotation matrix.

Similarly, we combine the local positions J_i and rotation angles ω_i^t of the remaining joints to obtain their local posed transformations:

$$B_{local_posed,i}^t = \begin{bmatrix} \mathbf{R}(\omega_i^t) & J_i \\ 0 & 1 \end{bmatrix}. \quad (21)$$

Next, we calculate the posed transformation for each joint in turn according to the connection order:

$$B_{posed,i}^t = B_{local_posed,i}^t B_{posed,parent(i)}^t, \quad (22)$$

where $parent(i)$ refers to the parent joint index of joint i . The calculation starts from the root joint.

In order to obtain the bone transformation from canonical space to posed space, we need the canonical transformations of joints. To simplify the calculation, we assume that the local rotation matrix of the canonical joints is the identity matrix, which can be achieved by preprocessing. We first calculate the local canonical transformations as follows:

$$B_{local_can,i}^t = \begin{bmatrix} I & J_i \\ 0 & 1 \end{bmatrix}. \quad (23)$$

As with Eq. 22, we compute the canonical transformation for each joint in turn:

$$B_{can,i}^t = B_{local_can,i}^t B_{can,parent(i)}^t. \quad (24)$$

Finally, we obtain the bone transformation mentioned in Eq. 7 by multiplying the inverse canonical transformation and the posed transformation:

$$B_i^t = B_{posed,i}^t \cdot (B_{can,i}^t)^{-1}. \quad (25)$$

Through the above calculation, we realized the mapping from the canonical joint positions \mathbf{J} , the posed rotation angle \mathbf{S}_t and the posed root translation T_t to the bone transformation \mathbf{B}_t . In other words, pose-guided deformation only relates to the joint position in canonical space. Therefore, we can implement different

deformations for different humans by optimizing joint positions in canonical space.

C Implementation Details

We extend the CUDA kernels of the 3D Gaussian rasterizer to achieve 3D Gaussian deformation and use the tiny-cuda-nn to implement the hash-encoded parameter field.

Network Architecture. To facilitate expansion, we build a hash-encoded network for each parameter. For spherical harmonic coefficients and vertex displacement, we use a hash table of length 2^{17} and a multi-layer perceptron with two hidden layers of 64 nodes each. For time-dependent ambient occlusion, we use a hash table of length 2^{19} and a multi-layer perceptron with two hidden layers of 64 nodes each.

Training Details. Since our method requires rapid convergence over several epochs, we set a fixed learning rate for each parameter. We use second-order spherical harmonics and optimize all coefficients at the beginning to speed up convergence. In order to learn both time-independent spherical harmonic colors and time-dependent ambient occlusion, we do not enable ambient occlusion until the fifth epoch.

D Additional Results

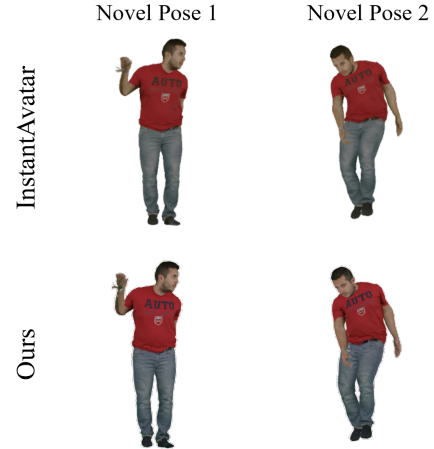


Figure 10: Novel Pose Results on PeopleSnapshot. Training 1 minute for InstantAvatar and 30 seconds for ours.